

Complete $\mathcal{O}(\alpha_s)$ QCD and $\mathcal{O}(\alpha_{ew})$ electroweak corrections to $t\bar{t}h^0$ production in $\gamma\gamma$ collision *

Chen Hui², Ma Wen-Gan^{1,2}, Zhang Ren-You², Zhou Pei-Jun², Hou Hong-Sheng² and Sun Yan-Bin²

¹ CCAST (World Laboratory), P.O.Box 8730, Beijing 100080, P.R.China

² Department of Modern Physics, University of Science and Technology of China (USTC), Hefei, Anhui 230027, P.R.China

Abstract

We calculate the full $\mathcal{O}(\alpha_s)$ QCD and $\mathcal{O}(\alpha_{ew})$ electroweak radiative corrections to the productions of a Higgs boson in intermediate mass region associated with $t\bar{t}$ pair in $\gamma\gamma$ collisions at an electron-positron linear collider (LC) in the standard model. We find the $\mathcal{O}(\alpha_s)$ QCD corrections can be larger than the $\mathcal{O}(\alpha_{ew})$ corrections depending on the Higgs boson mass m_h and e^+e^- colliding energy \sqrt{s} . Both kinds of corrections may significantly decrease or increase the Born cross sections. The numerical results show that the $\mathcal{O}(\alpha_s)$ QCD relative corrections to the process $e^+e^- \rightarrow \gamma\gamma \rightarrow t\bar{t}h^0$ can reach 34.8% when $\sqrt{s} = 800$ GeV and $m_h = 200$ GeV, while the $\mathcal{O}(\alpha_{ew})$ electroweak relative corrections to the Born cross sections can reach -13.1% , -15.8% and -12.0% at $\sqrt{s} = 800$ GeV, 1 TeV and 2 TeV, respectively.

PACS: 14.65.Ha, 14.80.Bn, 12.15.Lk, 12.38.Bx

Keywords: Associated Higgs boson production, QCD correction, electroweak correction, photon collider

*Supported by National Natural Science Foundation of China.

I Introduction

In the electroweak minimal standard model(MSM), Higgs mechanism generates electroweak symmetry breaking and the Yukawa coupling terms between Higgs boson and fermion in the Lagrangian [1, 2]. In the SM, the Yukawa term reads $\mathcal{L}_Y = -\sum_f m_f (1 + H(x)/v) \bar{\psi}_f \psi_f$. There the coupling strength of the fermion-Higgs Yukawa coupling $f - \bar{f} - h^0$ is predicted as $g_{f\bar{f}h} = m_f/v$ at the tree level, where $v = (\sqrt{2}G_F)^{-1/2} \simeq 246$ GeV is the vacuum expectation value of the Higgs field. Since the top quark is the heaviest fermion, the top quark Yukawa coupling $g_{t\bar{t}h}$ should be the strongest one among all the fermion-Higgs couplings, e.g., $g_{t\bar{t}h}^2 \simeq 0.5$ to be compared for example with $g_{b\bar{b}h}^2 \simeq 4 \times 10^{-4}$. Therefore, the Higgs boson production associated with a top-quark pair production process is particularly important in collider physics for probing the top-quark Yukawa coupling with Higgs boson in the intermediate mass range.

After the discovery of top quark, direct searching for Higgs boson and studying its property are the main goals of the high energy colliders. Recently, LEP2 experiments provided a lower bound of 114.4 GeV for the SM Higgs boson mass at the 95% confidence level[3]. The future linear colliders (LC) will continue the work in searching for Higgs bosons. There are already some detailed designs of linear colliders, such as NLC[4], JLC[5], TESLA[6] and CLIC[7]. Although the cross section for $e^+e^- \rightarrow t\bar{t}h^0$ process is small, about 1 fb for $\sqrt{s} = 500$ GeV and $m_h = 100$ GeV [8, 9, 10], it has a distinctive experimental signature and can potentially be used to measure the top-quark Yukawa coupling in the intermediate Higgs mass region at a LC with very high luminosity. The precise determination of the top-Higgs coupling via the measurement of $e^+e^- \rightarrow t\bar{t}h^0$ process can reach the accuracy of few percent

[11, 12, 13, 14]. S. Dawson and L. Reina gave the NLO QCD corrections to process $e^+e^- \rightarrow t\bar{t}h^0$ in Ref. [9]. And the full electroweak corrections to the process $e^+e^- \rightarrow t\bar{t}h^0$ were presented in references [15, 16, 17]. All these works show that the evaluation of radiative corrections is a crucial task for the accurate experimental measurements of this process.

An e^+e^- LC can also be designed to operate as a $\gamma\gamma$ collider. This is achieved by using Compton backscattered photons in the scattering of intense laser photons on the initial e^+e^- beams. The resulting $\gamma - \gamma$ center of mass system (CMS) energy is peaked at about $0.8\sqrt{s}$ for the appropriate choices of machine parameters. In $\gamma\gamma$ collision mode at the high energy peak, we may get approximately the same luminosity as that of e^+e^- collision. With the new possibility of $\gamma\gamma$ collisions at electron-positron linear colliders, the production process $e^+e^- \rightarrow \gamma\gamma \rightarrow t\bar{t}h^0$ offers another approach to probe directly the top-Higgs coupling in addition to $e^+e^- \rightarrow t\bar{t}h^0$ and $pp(p\bar{p}) \rightarrow t\bar{t}h^0$ processes. To detect the Higgs boson associated with a top-quark pair in high colliding energy, $\gamma\gamma$ collision has an outstanding advantage over e^+e^- collision due to its relative larger production rate. The reason is that at the tree level the $e^+e^- \rightarrow t\bar{t}h^0$ process has a ‘s-channel suppression’ from the virtual photon and Z^0 propagators, especially for the heavy masses of the final particles. Therefore, we can conclude that the $e^+e^- \rightarrow \gamma\gamma \rightarrow t\bar{t}h^0$ process with high colliding energy provides a better approach than e^+e^- collision to produce $t\bar{t}h^0$.

The Born cross section of $e^+e^- \rightarrow \gamma\gamma \rightarrow t\bar{t}h^0$ process was calculated already in previous work of Ref.[18]. In this paper we present the calculations of the full $\mathcal{O}(\alpha_s)$ QCD and $\mathcal{O}(\alpha_{\text{ew}})$ electroweak corrections to $e^+e^- \rightarrow \gamma\gamma \rightarrow t\bar{t}h^0$ in the SM, and compare our numerical results of Born cross sections of $e^+e^- \rightarrow \gamma\gamma \rightarrow t\bar{t}h^0$ with those in Ref.[18]. The paper is organized as follow. In section 2, we present

the notations and analytical calculations of the QCD and the electroweak radiative corrections. The numerical results and discussions are presented in section 3. Our conclusions are given in section 4. Some numerical comparison of the Born cross section of process $e^+e^- \rightarrow \gamma\gamma \rightarrow t\bar{t}h^0$ are presented in Appendix.

II Analytical Calculation

II.1 Calculations of the lowest order of the $\gamma\gamma \rightarrow t\bar{t}h^0$ subprocess

The subprocess $\gamma\gamma \rightarrow t\bar{t}h^0$ at the lowest level occurs through the u- and t-channel mechanisms involving Higgs boson bremsstrahlungs originated from different positions on top-quark lines. The tree level diagrams are shown in Fig.1, but the corresponding diagrams with interchange of the two incoming photons are not shown.

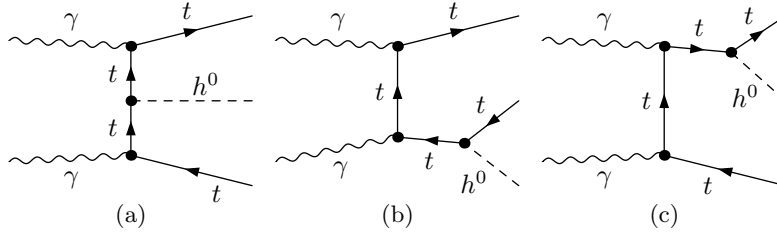


Figure 1: The lowest order diagrams for the $\gamma\gamma \rightarrow t\bar{t}h^0$ subprocess.

We define the kinematical variables of the subprocess $\gamma\gamma \rightarrow t\bar{t}h^0$ as

$$\gamma(p_1) + \gamma(p_2) \rightarrow t(k_1) + \bar{t}(k_2) + h^0(k_3). \quad (2.1)$$

The four-momenta of incoming electron and positron are denoted as p_1 and p_2 , respectively, and the four-momenta of outgoing top-quark, anti-top-quark and Higgs boson are represented as k_1 , k_2 and

k_3 correspondingly. All these momenta obey the on-shell equations $p_1^2 = p_2^2 = 0$, $k_1^2 = k_2^2 = m_t^2$ and $k_3^2 = m_h^2$.

The amplitudes of the corresponding t-channel Feynman diagrams (shown in Fig.1(a-c)) of the subprocess $\gamma\gamma \rightarrow t\bar{t}h^0$ are represented by

$$\begin{aligned} \mathcal{M}_t^{(a)} = & -\frac{e^3 Q_t^2 m_t}{2m_W \sin \theta_W} \frac{1}{(k_1 - p_1)^2 - m_t^2} \frac{1}{(p_2 - k_2)^2 - m_t^2} \\ & \times \bar{u}(k_1) \not{\epsilon}(p_1) (\not{k}_1 - \not{p}_1 + m_t) (\not{p}_2 - \not{k}_2 + m_t) \not{\epsilon}(p_2) v(k_2), \end{aligned} \quad (2.2)$$

$$\begin{aligned} \mathcal{M}_t^{(b)} = & -\frac{e^3 Q_t^2 m_t}{2m_W \sin \theta_W} \frac{1}{(k_1 - p_1)^2 - m_t^2} \frac{1}{(k_2 + k_3)^2 - m_t^2} \\ & \times \bar{u}(k_1) \not{\epsilon}(p_1) (\not{k}_1 - \not{p}_1 + m_t) \not{\epsilon}(p_2) (-\not{k}_2 - \not{k}_3 + m_t) v(k_2), \end{aligned} \quad (2.3)$$

$$\begin{aligned} \mathcal{M}_t^{(c)} = & -\frac{e^3 Q_t^2 m_t}{2m_W \sin \theta_W} \frac{1}{(k_1 + k_3)^2 - m_t^2} \frac{1}{(p_2 - q_2)^2 - m_t^2} \\ & \times \bar{u}(k_1) (\not{k}_1 + \not{k}_3 + m_t) \not{\epsilon}(p_1) (\not{p}_2 - \not{k}_2 + m_t) \not{\epsilon}(p_2) v(k_2), \end{aligned} \quad (2.4)$$

where $Q_t = 2/3$ and the corresponding amplitudes of the u-channel Feynman diagrams of the subprocess $\gamma\gamma \rightarrow t\bar{t}h^0$ can be obtained by the following interchanges.

$$\mathcal{M}_u^{(a)} = \mathcal{M}_t^{(a)}(p_1 \leftrightarrow p_2), \quad \mathcal{M}_u^{(b)} = \mathcal{M}_t^{(b)}(p_1 \leftrightarrow p_2), \quad \mathcal{M}_u^{(c)} = \mathcal{M}_t^{(c)}(p_1 \leftrightarrow p_2). \quad (2.5)$$

The total amplitude at the lowest order is the summation of the above amplitudes.

$$\mathcal{M}_0 = \sum_{i=a,b}^c \sum_{j=u}^t \mathcal{M}_j^{(i)}. \quad (2.6)$$

Although the previous calculations for the $\gamma\gamma \rightarrow t\bar{t}h^0$ subprocess and $e^+e^- \rightarrow \gamma\gamma \rightarrow t\bar{t}h^0$ process at the lowest order were presented by Kingman Cheung, we made the numerical comparison with the

results given in Ref.[18] yet. We calculated the Born cross section of the process $e^+e^- \rightarrow \gamma\gamma \rightarrow t\bar{t}h^0$ by using the packages *FeynArts* 3 [19] and *CompHep*[20] independently, and find our results are not coincident with Cheung's. We present the numerical comparison in Appendix.

II.2 Calculations of the Full $\mathcal{O}(\alpha_s)$ QCD corrections of the $\gamma\gamma \rightarrow t\bar{t}h^0$ subprocess

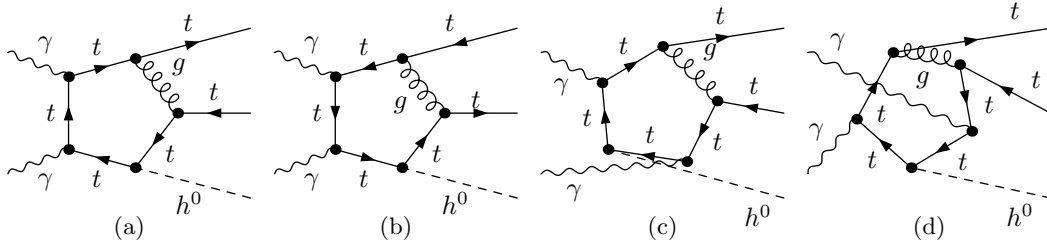


Figure 2: The QCD pentagon diagrams for the $\gamma\gamma \rightarrow t\bar{t}h^0$ subprocess, whose amplitudes include five-point tensor integrals of rank 4. The corresponding diagrams with interchange of the two incoming photons are not shown.

The $\mathcal{O}(\alpha_s)$ QCD one-loop Feynman diagrams of the subprocess $\gamma\gamma \rightarrow t\bar{t}h^0$ are generated by *FeynArts* 3 [19]. There are 84 Feynman diagrams with $\mathcal{O}(\alpha_s)$ corrections of the virtual one-loop QCD corrections, which involves the vertex correction, internal propagator self-energy correction, box and pentagon diagrams. The Feynman graphs which generate amplitudes including five-point integrals of rank 4 are shown in Fig.2 as a representative selection. The amplitude of the subprocess $\gamma\gamma \rightarrow t\bar{t}h^0$ including virtual QCD corrections to $\mathcal{O}(\alpha_s)$ can be expressed as

$$\mathcal{M}_{QCD} = \mathcal{M}_0 + \frac{\alpha_s}{4\pi} C_F \mathcal{M}_{QCD}^{vir}. \quad (2.7)$$

where $C_F = 4/3$, The term $\frac{\alpha_s}{4\pi} C_F \mathcal{M}_{QCD}^{vir}$ is the amplitude contributed by the QCD one-loop Feynman diagrams and the QCD renormalizations of top-quark wave function, mass and $t - \bar{t} - h^0$ Yukawa

coupling. We define the relevant renormalization constants as

$$m_{t,0} = m_t + \delta m_{t(g)}, \quad t_0^L = (1 + \frac{1}{2}\delta Z_{t(g)}^L)t^L, \quad t_0^R = (1 + \frac{1}{2}\delta Z_{t(g)}^R)t^R, \quad g_{t\bar{t}H}^0 = \frac{m_t}{v} + \frac{\delta m_{t(g)}}{v}. \quad (2.8)$$

With the on-shell renormalized condition we get the $\mathcal{O}(\alpha_s)$ QCD contributed parts of the renormalization constants as

$$\delta m_{t(g)} = \frac{m_t}{2} \tilde{Re} \left(\Sigma_{t(g)}^L(m_t^2) + \Sigma_{t(g)}^R(m_t^2) + 2\Sigma_{t(g)}^S(m_t^2) \right), \quad (2.9)$$

$$\delta Z_{t(g)}^L = -\tilde{Re} \Sigma_{t(g)}^L(m_t^2) - m_t^2 \frac{\partial}{\partial p^2} \tilde{Re} \left[\Sigma_{t(g)}^L(p^2) + \Sigma_{t(g)}^R(p^2) + 2\Sigma_{t(g)}^S(p^2) \right] \Big|_{p^2=m_t^2}, \quad (2.10)$$

$$\delta Z_{t(g)}^R = -\tilde{Re} \Sigma_{t(g)}^R(m_t^2) - m_t^2 \frac{\partial}{\partial p^2} \tilde{Re} \left[\Sigma_{t(g)}^L(p^2) + \Sigma_{t(g)}^R(p^2) + 2\Sigma_{t(g)}^S(p^2) \right] \Big|_{p^2=m_t^2}, \quad (2.11)$$

\tilde{Re} takes the real part of the loop integrals appearing in the self energies only. Here we define the renormalized top-quark irreducible two-point function as

$$\hat{\Gamma}_t(p^2) = i[\not{p}P_L \hat{\Sigma}_t^L(p^2) + \not{p}P_R \hat{\Sigma}_t^R(p^2) + m_t \hat{\Sigma}_t^S(p^2)] \delta_{\alpha\beta} \quad (2.12)$$

where α and β are the color indices of the top quarks on the two sides of the self-energy diagram, $P_{L,R} = (1 \mp \gamma_5)/2$. The unrenormalized top-quark self energy parts contributed by $\mathcal{O}(\alpha_s)$ QCD read

$$\Sigma_{t(g)}^L(p^2) = \Sigma_{t(g)}^R(p^2) = \frac{g_s^2}{6\pi^2} (-1 + 2B_0[p, 0, m_t] + 2B_1[p, 0, m_t]) \quad (2.13)$$

and

$$\Sigma_{t(g)}^S(p^2) = \frac{g_s^2}{3\pi^2} (1 - 2B_0[p, 0, m_t]) \quad (2.14)$$

The corresponding contribution part to the cross section at $\mathcal{O}(\alpha_s)$ order can be written as

$$\Delta\hat{\sigma}_{vir}^{QCD} = \hat{\sigma}_0\hat{\delta}_{vir}^{QCD} = \frac{\alpha_s C_F}{8\pi|\vec{p}_1|\sqrt{\hat{s}}} \int d\Phi_3 \overline{\sum_{\text{spin}}} \text{Re} \left(\mathcal{M}_0^\dagger \mathcal{M}_{QCD}^{vir} \right), \quad (2.15)$$

where $d\Phi_3$ is the three-body phase space element. The bar over summation recalls averaging over initial spins.

The virtual QCD corrections contain both ultraviolet (UV) and infrared (IR) divergences in general. To regularize the UV divergences in loop integrals, we adopt the dimensional regularization in which the dimensions of spinor and spacetime manifolds are extended to $D = 4 - 2\epsilon$. We have verified the cancellation of the UV both analytically and numerically. Then we get a UV finite amplitude including $\mathcal{O}(\alpha_s)$ virtual radiative corrections.

The IR divergence in the \mathcal{M}_{QCD}^{vir} of the process $\gamma\gamma \rightarrow t\bar{t}h^0$ is originated from virtual gluon corrections. It can be exactly cancelled by including the real gluon bremsstrahlung corrections to this subprocess in the soft gluon limit. The real gluon emission process is denoted as

$$\gamma(p_1) + \gamma(p_2) \rightarrow t(k_1) + \bar{t}(k_2) + h^0(k_3) + g(k), \quad (2.16)$$

where the real gluon radiates from the internal or external top(anti-top) quark line, and can be classified into two parts which behave soft and hard natures respectively. In order to isolate the soft photon emission singularity in the real gluon emission process, we adopt the general phase-space-slicing method [31], in which the bremsstrahlung phase space is divided into singular and non-singular regions. The cross section of the real gluon emission process (2.16) is decomposed into soft and hard terms

$$\Delta\hat{\sigma}_{real}^{QCD} = \Delta\hat{\sigma}_{soft}^{QCD} + \Delta\hat{\sigma}_{hard}^{QCD} = \hat{\sigma}_0(\hat{\delta}_{soft}^{QCD} + \hat{\delta}_{hard}^{QCD}). \quad (2.17)$$

We adopt the soft gluon approximation method with a cut ΔE in numerical calculations for the soft emission corrections ($k^0 < \Delta E$). With this approach the real gluon radiation from internal color lines does not lead to IR singularities and can be neglected in this approach. We find the contribution of the soft gluon emission process is [30, 32]

$$d\Delta\hat{\sigma}_{\text{soft}}^{QCD} = -d\hat{\sigma}_0 \frac{\alpha_s C_F}{2\pi^2} \int_{|\vec{k}| \leq \Delta E} \frac{d^3k}{2k^0} \left[\frac{k_1}{k_1 \cdot k} - \frac{k_2}{k_2 \cdot k} \right]^2, \quad (2.18)$$

in which ΔE is the energy cutoff of the soft gluon and $k^0 \leq \Delta E \ll \sqrt{s}$. $k^0 = \sqrt{|\vec{k}|^2 + m_g^2}$ is the gluon energy. Here we have introduced a small gluon mass m_g to regulate the infrared divergences occurring in the soft emission. The integral over the soft gluon phase space have been implemented, the analytical result of the soft gluon corrections to $\gamma\gamma \rightarrow t\bar{t}h^0 g$ is presented as[9]

$$\begin{aligned} \left(\frac{d\Delta\hat{\sigma}_{\text{soft}}^{QCD}}{dx_h} \right) &= \left(\frac{d\hat{\sigma}_0}{dx_h} \right) \frac{\alpha_s C_F}{2\pi} \left\{ -2 \log \left(\frac{4\Delta E^2}{m_g^2} \right) \left[1 - \frac{xk_1 \cdot k_2}{m_t^2(x^2 - 1)} \log(x^2) \right] - \frac{k_1^0}{|\vec{k}_1|} \log \left(\frac{k_1^0 - |\vec{k}_1|}{k_1^0 + |\vec{k}_1|} \right) \right. \\ &\quad - \frac{k_2^0}{|\vec{k}_2|} \log \left(\frac{k_2^0 - |\vec{k}_2|}{k_2^0 + |\vec{k}_2|} \right) + \frac{4xk_1 \cdot k_2}{m_t^2(x^2 - 1)} \left[\frac{1}{4} \log^2 \left(\frac{u^0 - |\vec{u}|}{u^0 + |\vec{u}|} \right) + \text{Li}_2 \left(1 - \frac{u^0 + |\vec{u}|}{v} \right) \right. \\ &\quad \left. \left. + \text{Li}_2 \left(1 - \frac{u^0 - |\vec{u}|}{v} \right) \right] \right\}_{u=xk_2}^{u=xk_1}, \end{aligned}$$

where

$$v = \frac{m_t^2(x^2 - 1)}{2(xk_1^0 - k_2^0)}, \quad (2.19)$$

and x is the solution of

$$m_t^2(x^2 + 1) - 2xk_1 \cdot k_2 = 0, \quad (2.20)$$

which should satisfy the constraint of

$$\frac{xk_1^0 - k_2^0}{k_2^0} > 0. \quad (2.21)$$

We checked numerically the cancellation of IR divergencies and verified that the contribution of these soft gluon bremsstrahlung corrections leads to an IR finite cross section which is independent of the infinitesimal gluon mass m_g . The hard gluon emission cross section $\Delta\hat{\sigma}_{\text{hard}}^{QCD}$ for $E_g > \Delta E$, is calculated numerically by using Monte Carlo method.

Finally the UV and IR finite total cross section of the subprocess $\gamma\gamma \rightarrow t\bar{t}h^0$ including the full $\mathcal{O}(\alpha_s)$ QCD corrections reads

$$\hat{\sigma}^{QCD} = \hat{\sigma}_0 + \Delta\hat{\sigma}^{QCD} = \hat{\sigma}_0 + \Delta\hat{\sigma}_{\text{vir}}^{QCD} + \Delta\hat{\sigma}_{\text{real}}^{QCD} = \hat{\sigma}_0(1 + \hat{\delta}^{QCD}), \quad (2.22)$$

where $\hat{\delta}^{QCD} = \hat{\delta}_{\text{vir}}^{QCD} + \hat{\delta}_{\text{soft}}^{QCD} + \hat{\delta}_{\text{hard}}^{QCD}$ is the full QCD relative correction of order $\mathcal{O}(\alpha_s)$.

II.3 The calculation of the full $\mathcal{O}(\alpha_{\text{ew}})$ corrections to the $\gamma\gamma \rightarrow t\bar{t}h^0$ subprocess

In addition to the QCD corrections, we also calculate the full $\mathcal{O}(\alpha_{\text{ew}})$ electroweak corrections to the subprocess $\gamma\gamma \rightarrow t\bar{t}h^0$. We use again the package *FeynArts3* [19] to generate the electroweak one-loop Feynman diagrams and the relevant amplitudes of the subprocess $\gamma\gamma \rightarrow t\bar{t}h^0$ automatically. The full electroweak one-loop Feynman diagrams can be classified into self-energy, triangle, box and pentagon diagrams. The pentagon diagrams, whose corresponding amplitudes include five-point tensor integrals of rank 4, are depicted in Fig.3 as a representative selection. In our electroweak correction calculation we use also the t'Hooft-Feynman gauge and adopt the definitions of one-loop integral functions of Ref.[27]. The one-loop level virtual electroweak corrections to $\gamma\gamma \rightarrow t\bar{t}h^0$ can be expressed as

$$\Delta\hat{\sigma}_{\text{vir}}^{EW} = \hat{\sigma}_0\hat{\delta}_{\text{vir}}^{EW} = \frac{N_c}{2|\vec{p}_1|\sqrt{\hat{s}}} \int d\Phi_3 \sum_{\text{spin}} \overline{\text{Re}} \left(\mathcal{M}_0^\dagger \mathcal{M}_{\text{vir}}^{EW} \right), \quad (2.23)$$

where \vec{p}_1 is the c.m.s. three-momentum of one of the incoming photons, $d\Phi_3$ is the three-body phase space element, and the bar over summation recalls averaging over initial spins. $\mathcal{M}_{\text{vir}}^{EW}$ is the amplitude of the electroweak one-loop Feynman diagrams, including self-energy, vertex, box, pentagon and counterterm diagrams.

Analogously to the case of the QCD correction calculations shown in last subsection, we adopt the dimensional regularization scheme to regularize the UV divergences in loop integrals. We assume that there is no quark mixing, the KM-matrix is identity matrix and use the complete on-mass-shell (COMS) renormalization scheme [30], in which the electric charge of electron e and the physical masses m_W , m_Z , m_h , m_t et al., are chosen to be the renormalized parameters. The relevant field renormalization constants are defined as [30]

$$\begin{aligned} e_0 &= (1 + \delta Z_e)e, \quad m_{h,0}^2 = m_h^2 + \delta m_h^2, \quad m_{t,0} = m_t + \delta m_t, \quad m_{W,0}^2 = m_W^2 + \delta m_W^2, \\ m_{Z,0}^2 &= m_Z^2 + \delta m_Z^2, \quad A_0 = \frac{1}{2}\delta Z_{AZ}Z + (1 + \frac{1}{2}\delta Z_{AA})A, \quad h_0 = (1 + \frac{1}{2}\delta Z_h)h, \\ t_0^L &= (1 + \frac{1}{2}\delta Z^L)t^L, \quad t_0^R = (1 + \frac{1}{2}\delta Z^R)t^R. \end{aligned} \quad (2.24)$$

With the on-mass-shell conditions, we can obtain the renormalized constants expressed as

$$\begin{aligned} \delta m_W^2 &= \tilde{R}e\Sigma_T^W(m_W^2), \quad \delta m_Z^2 = Re\Sigma_T^{ZZ}(m_Z^2), \quad \delta Z_{AA} = -\frac{\partial \Sigma_T^{AA}(p^2)}{\partial p^2}|_{p^2=0}, \\ \delta Z_{ZZ} &= -Re\frac{\partial \Sigma_T^{ZZ}(p^2)}{\partial p^2}|_{p^2=m_Z^2}, \quad \delta Z_{ZA} = 2\frac{\Sigma_T^{ZA}(0)}{m_Z^2}, \quad \delta Z_{AZ} = -2Re\frac{\Sigma_T^{AZ}(m_Z^2)}{m_Z^2}, \\ \delta m_h &= Re\Sigma^h(m_h^2), \quad \delta Z_h = -Re\frac{\partial \Sigma^h(p^2)}{\partial p^2}|_{p^2=m_h^2}. \end{aligned} \quad (2.25)$$

The renormalization constants of the wave function and mass of top-quark can be evaluated from Eqs.(2.9)-(2.11) upon replacing the QCD top-quark self-energies($\Sigma_{t(g)}^L$, $\Sigma_{t(g)}^R$ and $\Sigma_{t(g)}^S$) by the elec-

troweak corresponding ones (Σ_t^L , Σ_t^R and Σ_t^S), respectively. And the explicit expressions of the electroweak self energies in the SM concerned in our calculations can be found in the Appendix B of Ref.[30]. The UV divergence appearing from the one-loop diagrams is cancelled by the contributions of the counterterm diagrams in our calculations. We have verified both analytically and numerically that the final cross sections including $\mathcal{O}(\alpha_{ew})$ virtual radiative corrections and the corresponding counterterm contributions are UV finite.

Analogous to the calculation of the QCD corrections, the IR divergence in the subprocess $\gamma\gamma \rightarrow t\bar{t}h^0$ originates from virtual photonic corrections is cancelled by the real photonic bremsstrahlung corrections in the soft photon limit. We use also the general phase-space-slicing method [31] and divide the phase space into singular and non-singular regions. Then the cross section of the real photon emission subprocess ($\gamma\gamma \rightarrow t\bar{t}h^0\gamma$) is decomposed into soft and hard parts.

$$\Delta\hat{\sigma}_{\text{real}} = \Delta\hat{\sigma}_{\text{soft}} + \Delta\hat{\sigma}_{\text{hard}} = \hat{\sigma}_0(\hat{\delta}_{\text{soft}}^\gamma + \hat{\delta}_{\text{hard}}^\gamma). \quad (2.26)$$

By using the soft photon($k^0 < \Delta E$) approximation, we get the contribution of the soft photon emission subprocess expressed as [30, 32]

$$d\Delta\hat{\sigma}_{\text{soft}}^\gamma = -d\hat{\sigma}_0 \frac{\alpha_{ew} Q_t^2}{2\pi^2} \int_{|\vec{k}| \leq \Delta E} \frac{d^3k}{2k_0} \left[\frac{k_1}{k_1 \cdot k} - \frac{k_2}{k_2 \cdot k} \right]^2, \quad (2.27)$$

in which ΔE is the energy cutoff of the soft photon and $k^0 \leq \Delta E \ll \sqrt{\hat{s}}$, $Q_t = 2/3$ is the electric charges of top quark, $k^0 = \sqrt{|\vec{k}|^2 + m_\gamma^2}$ is the photon energy. Therefore, after the integration over the soft photon phase space, we obtain the analytical result of the soft corrections to $\gamma\gamma \rightarrow t\bar{t}h^0$. Actually, the real photonic emission correction can be deduced from the real gluon emission corrections upon replacing the factor $C_F\alpha_s$ by $Q^2\alpha_{ew}$. The cancellation of IR divergencies is verified and the results of

the cross section show the independence on the infinitesimal photon mass m_γ in our calculation.

Since sometimes the QED radiative contributions can be quite large, the investigation of the genuine weak corrections quantitatively would help us to understand the origination of the large electroweak corrections. The QED corrections to the subprocess $\gamma\gamma \rightarrow t\bar{t}h^0$ is gauge invariant and comprise three parts: (1) photonic virtual radiations of final and internal top-quarks, (2) real photonic radiations from final and internal top-quarks, (3) the interference of final and internal real photon radiations. Actually, the total $\mathcal{O}(\alpha_{ew})$ order QED corrections for the subprocess $\gamma\gamma \rightarrow t\bar{t}h^0$, can be obtained numerically from the results of the $\mathcal{O}(\alpha_s)$ order QCD corrections as presented in section II.2 through multiplying a factor of $\frac{\alpha_{ew}Q_t^2}{\alpha_s(\mu)C_F}$. Then the genuine weak corrections can be evaluated by subtracting the QED corrections from the full $\mathcal{O}(\alpha_{ew})$ QED corrections. We define the genuine weak relative correction as,

$$\hat{\delta}_w = \hat{\delta} - \hat{\delta}^{QED} = \hat{\delta} - \hat{\delta}_{vir}^{QED} - \hat{\delta}_{soft}^{QED} - \hat{\delta}_{hard}^{QED}. \quad (2.28)$$

where $\hat{\delta}_{vir}^{QED}$ is the relative correction contributed by the QED one-loop diagrams including virtual photon exchange and the corresponding parts of the counter terms. $\hat{\delta}_{soft}^{QED}$ and $\hat{\delta}_{hard}^{QED}$ are the relative corrections of the soft and hard real photon emissions, respectively.

II.4 Calculations of process $e^+e^- \rightarrow \gamma\gamma \rightarrow t\bar{t}h^0$

By using the laser back-scattering technique on an electron- or positron-beam, an e^+e^- LC which has c.m.s. energy of hundred GeV to several TeV can be transformed to be a photon collider [22, 23, 24]. By integrating over the photon luminosity in an e^+e^- linear collider, the total cross section of the

process $e^+e^- \rightarrow \gamma\gamma \rightarrow t\bar{t}h^0$ can be obtained in the form as

$$\sigma(s) = \int_{E_0/\sqrt{s}}^{x_{max}} dz \frac{d\mathcal{L}_{\gamma\gamma}}{dz} \hat{\sigma}(\gamma\gamma \rightarrow t\bar{t}h \text{ at } \hat{s} = z^2 s) \quad (2.29)$$

where $E_0 = 2m_t + m_h$, and $\sqrt{s}(\sqrt{\hat{s}})$ being the $e^+e^- (\gamma\gamma)$ c.m.s. energy. $\frac{d\mathcal{L}_{\gamma\gamma}}{dz}$ is the distribution function of photon luminosity, which is defined as:

$$\frac{d\mathcal{L}_{\gamma\gamma}}{dz} = 2z \int_{z^2/x_{max}}^{x_{max}} \frac{dx}{x} F_{\gamma/e}(x) F_{\gamma/e}(z^2/x) \quad (2.30)$$

For the initial unpolarized electrons and laser photon beams, the energy spectrum of the back scattered photon is given by [25]

$$F_{\gamma/e} = \frac{1}{D(\xi)} \left[1 - x + \frac{1}{1-x} - \frac{4x}{\xi(1-x)} + \frac{4x^2}{\xi^2(1-x)^2} \right] \quad (2.31)$$

where $x = 2\omega/\sqrt{s}$ is the fraction of the energy of the incident electron carried by the back-scattered photon, the maximum fraction of energy carried by the back-scattered photon is $x_{max} = 2\omega_{max}/\sqrt{s} = \xi/(1+\xi)$, and

$$D(\xi) = \left(1 - \frac{4}{\xi} - \frac{8}{\xi^2}\right) \ln(1+\xi) + \frac{1}{2} + \frac{8}{\xi} - \frac{1}{2(1+\xi)^2}, \quad (2.32)$$

$$\xi = \frac{2\sqrt{s}\omega_0}{m_e^2}. \quad (2.33)$$

m_e and $\sqrt{s}/2$ are the mass and energy of the electron, ω_0 is the laser-photon energy. In our evaluation, we choose ω_0 such that it maximizes the backscattered photon energy without spoiling the luminosity through e^+e^- pair creation. Then we have $\xi = 2(1 + \sqrt{2})$, $x_{max} \simeq 0.83$, and $D(\xi) \approx 1.84$, as used in Ref.[26].

III Numerical results and discussions

For the numerical calculation we use the following input parameters [33]

$$\begin{array}{llll}
\alpha_{\text{ew}}(0)^{-1} & = & 137.03599976, & m_W = 80.423 \text{ GeV}, & m_Z = 91.1876 \text{ GeV}, \\
m_e & = & 0.510998902 \text{ MeV}, & m_\mu = 105.658357 \text{ MeV}, & m_\tau = 1.77699 \text{ GeV}, \\
m_u & = & 66 \text{ MeV}, & m_c = 1.2 \text{ GeV}, & m_t = 174.3 \text{ GeV}, \\
m_d & = & 66 \text{ MeV}, & m_s = 150 \text{ MeV}, & m_b = 4.3 \text{ GeV}, \\
\alpha_s(m_Z^2) & = & 0.117186.
\end{array}$$

where we use the effective values of the light quark masses (m_u and m_d) which can reproduce the hadron contribution to the shift in the fine structure constant $\alpha_{\text{ew}}(m_Z^2)$ [34]. The QCD renormalization scale μ is taken as $(2m_t + m_h)/2$ and the running of the strong coupling $\alpha_s(\mu^2)$ is evaluated at the two-loop level (\overline{MS} scheme) with five flavors.

The numerical results of the cross sections with QCD and one-loop electroweak radiative corrections for the subprocess $\gamma\gamma \rightarrow t\bar{t}h^0$ are plotted in Fig.4 and Fig.5, respectively. The full, dashed, and dash-dotted curves correspond to the cases when $m_h = 115, 150$ and 200 GeV , correspondingly, and $\gamma\gamma$ colliding energy $\sqrt{\hat{s}}$ runs from the value little larger than the threshold $(2m_t + m_h)$ to 1.8 TeV . For each line type there are two curves, the upper curve (in the region $\sqrt{\hat{s}} > 1 \text{ TeV}$) is for the Born cross section and the lower one for the QCD corrected cross section. As indicated in Fig.4, the QCD corrections can increase (when $\sqrt{\hat{s}} < 650 \text{ GeV}$) or decrease the cross sections of subprocess $\gamma\gamma \rightarrow t\bar{t}h^0$ (when $\sqrt{\hat{s}} > 900 \text{ GeV}$), while Fig.5 shows that the one-loop electroweak radiative corrections always reduce the Born cross sections in the plotted energy range of $\sqrt{\hat{s}}$. All the curves in both Fig.4 and Fig.5 show that all the Born, QCD and electroweak corrected cross sections decrease with the increment of the mass of Higgs boson m_h . The curves for $m_h = 115 \text{ GeV}$ increase rapidly to their corresponding

maximal cross section values, when the $\gamma\gamma$ colliding energy $\sqrt{\hat{s}}$ goes from the threshold value to the corresponding position of peak. The curves for $m_h = 150$ GeV have platforms when $\sqrt{\hat{s}}$ are larger than 1000 GeV, and for $m_h = 200$ GeV both Born and one-loop corrected cross sections increase slowly in the whole plotted range of $\sqrt{\hat{s}}$.

We define the QCD relative corrections to the subprocess $\gamma\gamma \rightarrow t\bar{t}h^0$ and parent process $e^+e^- \rightarrow \gamma\gamma \rightarrow t\bar{t}h^0$ as

$$\hat{\delta}^{QCD} = \frac{\hat{\sigma}^{QCD} - \hat{\sigma}_0}{\hat{\sigma}_0}, \quad \delta^{QCD} = \frac{\sigma^{QCD} - \sigma_0}{\sigma_0}, \quad (3.1)$$

respectively, and the electroweak relative corrections to the subprocess $\gamma\gamma \rightarrow t\bar{t}h^0$ and process $e^+e^- \rightarrow \gamma\gamma \rightarrow t\bar{t}h^0$ as

$$\hat{\delta} = \frac{\hat{\sigma} - \hat{\sigma}_0}{\hat{\sigma}_0}, \quad \delta = \frac{\sigma - \sigma_0}{\sigma_0}, \quad (3.2)$$

correspondingly. The $\mathcal{O}(\alpha_s)$ QCD relative corrections and $\mathcal{O}(\alpha_{ew})$ electroweak relative corrections to the cross section for $\gamma\gamma \rightarrow t\bar{t}h^0$ subprocess, corresponding to Fig.4 and Fig.5, are depicted in Fig.6 and Fig.7(a-b), respectively. We can read from Fig.6 that the QCD relative corrections to the subprocess $\gamma\gamma \rightarrow t\bar{t}h^0$ decrease from 111% to -13.8% when the c.m.s. energy $\sqrt{\hat{s}}$ increases from the threshold energy to 1.8 TeV. From Fig.7(a) we can see that in the plotted colliding energy range, the $\mathcal{O}(\alpha_{ew})$ order electroweak relative corrections to subprocess $\gamma\gamma \rightarrow t\bar{t}h^0$ can reach -7.98% and -16.5% for $m_h = 115$ GeV and 200 GeV, respectively. The maximal electroweak absolute relative corrections to the cross sections $|\hat{\delta}|_{max}$ and the corresponding $\sqrt{\hat{s}}$ positions for subprocess $\gamma\gamma \rightarrow t\bar{t}h^0$ with $m_h = 115, 130, 150, 170, 200$ GeV are listed in Table 1. In Fig.7(b) the $\mathcal{O}(\alpha_{ew})$ order QED and genuine weak

relative corrections are depicted, respectively. It shows that the $\mathcal{O}(\alpha_{ew})$ QED relative corrections are very small comparing with the genuine weak relative corrections, and can only reach 1.28% for the curve with $\sqrt{\hat{s}} \sim 580 \text{ GeV}$ and $m_h = 200 \text{ GeV}$.

We also depicted the QCD and electroweak relative corrections to the cross sections of subprocess $\gamma\gamma \rightarrow t\bar{t}h^0$ as the functions of the mass of Higgs boson m_h with $\sqrt{\hat{s}} = 500, 800, 1000, 2000 \text{ GeV}$ in Fig.8 and Fig.9, respectively. Both curves for $\sqrt{\hat{s}} = 500 \text{ GeV}$ in Fig.8 and Fig.9 stop approximately at the position near $m_h \sim 150 \text{ GeV}$, because the subprocess $\gamma\gamma \rightarrow t\bar{t}h^0$ cannot be opened when $\sqrt{\hat{s}} < m_h + 2m_t$. On the curves for $\sqrt{\hat{s}} = 800, 1000, 2000 \text{ GeV}$ in Fig.9, there exist two resonance peaks on each curve at the positions $m_h \sim 2m_Z$ and $m_h \sim 2m_W$ due to the resonance effects. In Fig.8, the QCD relative corrections for $\sqrt{\hat{s}} = 500 \text{ GeV}$ are rather large, and can reach the value larger than 110% when the threshold energy of $t\bar{t}h^0$ is near 500 GeV, while the QCD relative corrections are in the range $1.74\% \sim -14.0\%$, when $\sqrt{\hat{s}} = 800, 1000, 2000 \text{ GeV}$. Fig.9 shows that the curves of the electroweak relative corrections for $\sqrt{\hat{s}} = 800 \text{ GeV}$ and 1000 GeV go down from -6.48% to -16.0% and from -7.01% to -13.9% respectively, when m_h varies from 100 GeV to 200 GeV. While the electroweak relative corrections for $\sqrt{\hat{s}} = 2000 \text{ GeV}$ are relative stable(about minus a few percent) except in the Higgs mass regions satisfying resonance conditions.

Fig.10 and Fig.11 show the cross sections including $\mathcal{O}(\alpha_s)$ QCD and $\mathcal{O}(\alpha_{ew})$ radiative corrections and for $e^+e^- \rightarrow \gamma\gamma \rightarrow t\bar{t}h^0$ process versus the e^+e^- colliding energy \sqrt{s} , respectively. Both figures demonstrate that the Born and radiative corrected cross sections increase with the increment of \sqrt{s} , and the $\mathcal{O}(\alpha_s)$ QCD radiative corrections for different values of m_h can reduce or increase the Born cross sections, but the $\mathcal{O}(\alpha_{ew})$ electroweak corrections reduce the Born cross section only in the plotted

range of electron-positron c.m.s. energy \sqrt{s} . The QCD and electroweak relative corrections for the $e^+e^- \rightarrow \gamma\gamma \rightarrow t\bar{t}h^0$ process corresponding to Fig.10 and Fig.11, are depicted in Fig.12 and Fig.13, respectively. We can see that the QCD relative correction can be very large near the threshold colliding energy, while the electroweak relative corrections can reach -15.9% for $m_h = 200$ GeV in the vicinity of $\sqrt{s} \sim 1$ TeV. The maximum absolute electroweak relative corrections for different Higgs boson mass values in the plotted colliding c.m.s. energy range can be read out from this figure and are listed in Table 2.

The QCD and electroweak relative corrections to the cross section of the process $e^+e^- \rightarrow \gamma\gamma \rightarrow t\bar{t}h^0$ as the functions of the Higgs boson mass m_h are depicted in Fig.14 and Fig.15 with $\sqrt{s} = 800, 1000, 2000$ GeV, respectively. From Fig.14 we can see that the QCD one-loop relative correction for $\sqrt{s} = 800$ GeV can reach 34.8% at the position of $m_h = 200$ GeV. In Fig.15 two resonance peaks appear again on each curve at the positions of $m_h \sim 2m_Z$ and $m_h \sim 2m_W$ because of the resonance effects. For the curves of $m_h = 800$ GeV and $m_h = 1000$ GeV, the relative correction decrease from -2.66% and -4.51% to -13.1% and -15.9% , respectively, when m_h varies from 100 GeV to 200 GeV. The relative correction for $\sqrt{s} = 2000$ GeV are varying in the range of $[-6.15\%, -12.0\%]$ when m_h goes from 100 GeV to 200 GeV, except in the h^0 mass regions satisfying the resonance effect conditions.

IV Summary

In this paper we calculate the complete $\mathcal{O}(\alpha_s)$ QCD and $\mathcal{O}(\alpha_{\text{ew}})$ electroweak radiative corrections to the $e^+e^- \rightarrow \gamma\gamma \rightarrow t\bar{t}h^0$ process with Higgs boson in intermediate mass region at an e^+e^- linear collider (LC) in the SM. We investigate the dependence of the QCD and electroweak radiative corrections to

both subprocess $\gamma\gamma \rightarrow t\bar{t}h^0$ and parent process $e^+e^- \rightarrow \gamma\gamma \rightarrow t\bar{t}h^0$ on the Higgs boson mass m_h and colliding energy $\sqrt{\hat{s}}$ (\sqrt{s}), and find that the QCD corrections can either increase or decrease the Born cross sections, while the electroweak corrections always decrease the Born cross sections of the $e^+e^- \rightarrow \gamma\gamma \rightarrow t\bar{t}h^0$ parent process and $\gamma\gamma \rightarrow t\bar{t}h^0$ subprocess in the Higgs boson mass range $115 \text{ GeV} < m_h < 200 \text{ GeV}$. We find also the $\mathcal{O}(\alpha_s)$ QCD corrections to process $e^+e^- \rightarrow \gamma\gamma \rightarrow t\bar{t}h^0$ can be larger than the $\mathcal{O}(\alpha_{\text{ew}})$ corrections depending on the Higgs boson mass m_h and e^+e^- colliding energy \sqrt{s} , Both kinds of corrections may significantly decrease or increase the Born cross sections. The numerical results show that the $\mathcal{O}(\alpha_s)$ QCD relative corrections to the process $e^+e^- \rightarrow \gamma\gamma \rightarrow t\bar{t}h^0$ can reach 34.8% when $\sqrt{s} = 800 \text{ GeV}$ and $m_h = 200 \text{ GeV}$, while the $\mathcal{O}(\alpha_{\text{ew}})$ electroweak relative corrections to the Born cross sections can reach -13.1% , -15.8% and -12.0% at $\sqrt{s} = 800 \text{ GeV}$, 1 TeV and 2 TeV , respectively.

Acknowledgments: This work was supported in part by the National Natural Science Foundation of China and a grant from the University of Science and Technology of China.

Appendix

In Appendix we list the numerical comparison of the cross sections at the tree level for the process $e^+e^- \rightarrow \gamma\gamma \rightarrow t\bar{t}h^0$. In order to check our calculation we use two independent packages *FeynArts* 3[19] and CompHep[20] to evaluate the cross sections. The results of ours and Kingman Cheung's [18] are presented in Table 3. It is clear that our cross sections at tree level are not coincident with Cheung's results.

References

- [1] S. L. Glashow, Nucl. Phys. **22**, 579 (1961); S. Weinberg, Phys. Rev. Lett. **1**, 1264 (1967); A. Salam, Proc. 8th Nobel Symposium Stockholm 1968, ed. N. Svartholm(Almquist and Wiksells, Stockholm 1968) p.367; H. D. Politzer, Phys. Rep. **14**, 129 (1974).
- [2] P. W. Higgs, Phys. Lett. **12**, 132 (1964); Phys. Rev. Lett. **13**, 508 (1964); Phys. Rev. **145**, 1156 (1966); F. Englert and R. Brout, Phys. Rev. Lett. **13**, 321 (1964); G. S. Guralnik, C. R. Hagen and T. W. B. Kibble, Phys. Rev. Lett. **13**, 585 (1964); T. W. B. Kibble, Phys. Rev. **155**, 1554 (1967).
- [3] ALEPH, DELPHI, L3 and OPAL Collaborations, The LEP working group for Higgs boson search, LHWG Note 2002-01 (July 2002), contributed paper for ICHEP'02 (Amsterdam, July 2002), and additional updates at <http://lephiggs.web.cern.ch/LEPHIGGS/www/Welcome.html>; P. A. McNamara and S. L. Wu, Rept. Prog. Phys. **65**, 465 (2002).
- [4] C. Adolphsen *et al.*, (International Study Group Collaboration), “International study group progress report on linear collider development”, SLAC-R-559 and KEK-REPORT-2000-7 (April, 2000).
- [5] N. Akasaka *et al.*, “JLC design study”, KEK-REPORT-97-1.
- [6] R. Brinkmann, K. Flottmann, J. Rossbach, P. Schmuser, N. Walker and H. Weise(editor), “TESLA: The superconducting electron positron linear collider with an integrated X-ray laser laboratory. Technical design report, Part 2: The Accelerator”, DESY-01-11 (March, 2001).

- [7] “A 3 TeV e^+e^- Linear Collider Based on CLIC Technology”, G. Guignard(editor), CERN-2000-008.
- [8] S. Dittmaier, M. Krämer, Y. Liao, M. Spira and P. M. Zerwas, Phys. Lett. **B441**, 383 (1998).
- [9] S. Dawson and L. Reina, Phys. Rev. **D59**, 054012 (1999), arXiv:hep-ph/9808443.
- [10] A. Juste and G. Merino, arXiv:hep-ph/9910301.
- [11] T. Abe et al. [American Linear Collider Working Group Collaboration], “Linear collider physics resource book for Snowmass 2001”, in Proc. of the APS/DPF/DPB Summer Study on the Future of Particle Physics (Snowmass 2001) arXiv:hep-ex/106055, arXiv:hep-ex/106057, arXiv:hep-ex/106058.
- [12] J. A. Aguilar-Saavedra et al. [ECFA/DESY LC Physics Working Group Collaboration], “TESLA Technical Design Report Part III:Physics at an e^+e^- -Linear Collider”, arXiv:hep-ph/0106315.
- [13] K. Abe et al., [ACFA Linear Collider Working Group Collaboration], “Particle physics experiments at JLC”, arXiv:hep-ph/0109166.
- [14] M. Battaglia and K. Desch, arXiv:hep-ph/0101165 and references therein.
- [15] Y. You, W.-G. Ma, H. Chen, R.-Y. Zhang, Y.-B. Sun, H.-S. Hou, arXiv:hep-ph/0306036.
- [16] G. Belanger, F. Boudjema, J. Fujimoto, T. Ishikawa, T. Kaneko, K. Kato, Y. Shimizu and Y. Yasui, arXiv:hep-ph/0307029.
- [17] A. Denner, S. Dittmaier, M. Roth, M. M. Weber, arXiv:hep-ph/0307193.

- [18] Kingman Cheung, Phys. Rev. D **47** (1993) 3750, arXiv:hep-ph/9211262.
- [19] T. Hahn, Comp. Phys. Commun. **140**, 418 (2001).
- [20] A.Pukhov, E.Boos, et al., “CompHEP - a package for evaluation of Feynman diagrams and integration over multi-particle phase space. User’s manual for version 33”, arXiv:hep-ph/9908288.
- [21] G.P. Lepage, J. Comput. Phys. **27** (1978)192 and CLNS-80/447.
- [22] I. Ginzburg, G. Kotkin, V. Serbo and V. Telnov, Pisma ZhETF, **34** (1981) 514; JETP Lett. **34** (1982) 491. Preprint INP 81-50, 1981, Novosibirsk.
- [23] I. Ginzburg, G. Kotkin, V. Serbo and V. Telnov, Nucl. Instr. & Meth. **205** (1983) 47, Preprint INP 81-102, 1991, Novosibirsk.
- [24] I. Ginzburg, G. Kotkin, S. Panfil, V. Serbo and V. Telnov, Nucl. Instr. & Meth. **219** (1984) 5.
- [25] V. Telnov, Nucl. Instrum. Methods Phys. Res. **A294**(1990)72; L. Ginzburg, G. Kotkin and H. Spiesberger, Fortschr. Phys. **34**(1986)687.
- [26] K. Cheung, Phys.Rev. **D47**(1993)3750.
- [27] G. Passarino and M. Veltman, Nucl. Phys. **B160**, 151 (1979).
- [28] A. Denner and S. Dittmaier, Nucl.Phys. **B658**, 175 (2003).
- [29] G. 't Hooft and M. Veltman, Nucl. Phys. **B44**, 189 (1972).
- [30] A. Denner, Fortschr. Phys. **41**, 307 (1993).

- [31] W. T. Giele and E. W. Glover, Phys. Rev. **D46**, 1980 (1992); W. T. Giele, E. W. Glover and D. A. Kosower, Nucl. Phys. **B403**, 633 (1993); S. Keller and E. Laenen, Phys. Rev. **D59**, 114004 (1999).
- [32] G.'t Hooft and M. Veltman, Nucl. Phys. **B153**, 365 (1979).
- [33] K. Hagiwara, *et al.*, Phy. Rev. **D66**, 1 (2002).
- [34] F. Legerlehner, DESY 01-029, arXiv:hep-ph/0105283.

Figure Captions

Figure 1 The lowest order diagrams for the $\gamma\gamma \rightarrow t\bar{t}h^0$ subprocess..

Figure 2 The QCD pentagon diagrams for the $\gamma\gamma \rightarrow t\bar{t}h^0$ subprocess, whose amplitudes include five-point tensor integrals of rank 4. The corresponding diagrams with interchange of the two incoming photons are not shown.

Figure 3 The five-point pentagon electroweak one-loop diagrams for the $\gamma\gamma \rightarrow t\bar{t}h^0$ subprocess, whose corresponding amplitudes include five-point tensor integrals of rank 4.

Figure 4 The Born and one-loop QCD corrected cross sections for the $\gamma\gamma \rightarrow t\bar{t}h^0$ subprocess as the functions of c.m.s. energy ($\sqrt{\hat{s}}$) with $m_h = 115, 150, 200$ GeV, respectively. For each line type, the upper curve (in the energy region $\sqrt{\hat{s}} > 1$ TeV) is for the Born cross section and the lower one for the one-loop QCD corrected cross section.

Figure 5 The Born and one-loop electroweak corrected cross sections for the $\gamma\gamma \rightarrow t\bar{t}h^0$ subprocess as the functions of c.m.s. energy ($\sqrt{\hat{s}}$) with $m_h = 115, 150, 200$ GeV. For each line type, the upper

curve is for the Born cross section and the lower one for the one-loop electroweak corrected cross section.

Figure 6 The QCD one-loop relative corrections as the functions of c.m.s. energy ($\sqrt{\hat{s}}$) for the $\gamma\gamma \rightarrow t\bar{t}h^0$ subprocess with $m_h = 115, 150, 200$ GeV, respectively.

Figure 7 (a)The electroweak one-loop relative corrections as the functions of c.m.s. energy ($\sqrt{\hat{s}}$) with $m_h = 115, 150, 200$ GeV for the $\gamma\gamma \rightarrow t\bar{t}h^0$ subprocess. (b)The QED and weak one-loop relative corrections as the functions of c.m.s. energy ($\sqrt{\hat{s}}$) with $m_h = 115, 150, 200$ GeV for the $\gamma\gamma \rightarrow t\bar{t}h^0$ subprocess. For each line type, the upper curve is for the QED corrected cross section and the lower one for the weak corrected cross section.

Figure 8 The QCD one-loop relative corrections as the functions of the mass of Higgs boson (m_h) for the $\gamma\gamma \rightarrow t\bar{t}h^0$ subprocess with $\sqrt{\hat{s}} = 500, 800, 1000, 2000$ GeV, respectively.

Figure 9 The electroweak one-loop relative corrections as the functions of the mass of Higgs boson (m_h) for the $\gamma\gamma \rightarrow t\bar{t}h^0$ subprocess with $\sqrt{\hat{s}} = 500, 800, 1000, 2000$ GeV, respectively.

Figure 10 The Born and one-loop QCD corrected cross sections for the $e^+e^- \rightarrow \gamma\gamma \rightarrow t\bar{t}h^0$ process as the functions of c.m.s. energy (\sqrt{s}) with $m_h = 115, 150, 200$ GeV, respectively. For each line type, the upper curve(in the energy region $\sqrt{s} > 1.4$ TeV) is for the Born cross section and the lower one presents the one-loop corrected cross section.

Figure 11 The Born and one-loop electroweak corrected cross sections for the $e^+e^- \rightarrow \gamma\gamma \rightarrow t\bar{t}h^0$ process as the functions of c.m.s. energy (\sqrt{s}) with $m_h = 115, 150, 200$ GeV, respectively. For each line type, the upper curve is for the Born cross section and the lower one presents the one-loop corrected cross section.

Figure 12 The QCD one-loop relative corrections to the $e^+e^- \rightarrow \gamma\gamma \rightarrow t\bar{t}h^0$ process as the functions of c.m.s. energy (\sqrt{s}) with $m_h = 115, 150, 200$ GeV, respectively.

Figure 13 The electroweak one-loop relative corrections to the $e^+e^- \rightarrow \gamma\gamma \rightarrow t\bar{t}h^0$ process as the functions of c.m.s. energy (\sqrt{s}) with $m_h = 115, 150, 200$ GeV, respectively.

Figure 14 The QCD one-loop relative corrections to the $e^+e^- \rightarrow \gamma\gamma \rightarrow t\bar{t}h^0$ process as the functions of Higgs boson mass (m_h) with $\sqrt{s} = 800, 1000, 2000$ GeV.

Figure 15 The electroweak one-loop relative corrections as the functions of Higgs boson mass (m_h) with $\sqrt{s} = 800, 1000, 2000$ GeV, respectively.

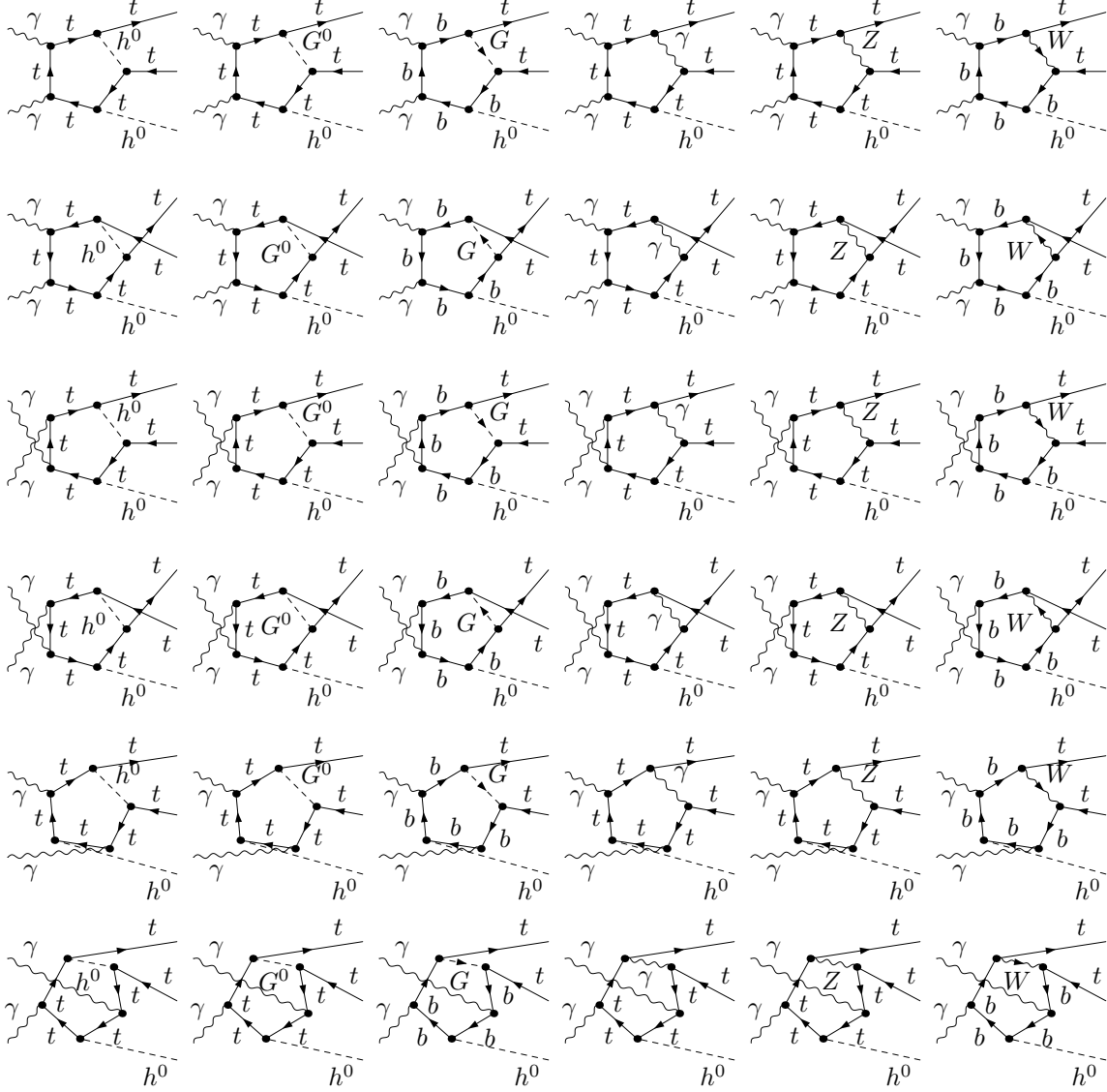


Figure 3: The five-point pentagon electroweak one-loop diagrams for the $\gamma\gamma \rightarrow t\bar{t}h^0$ subprocess, whose corresponding amplitudes include five-point tensor integrals of rank 4.

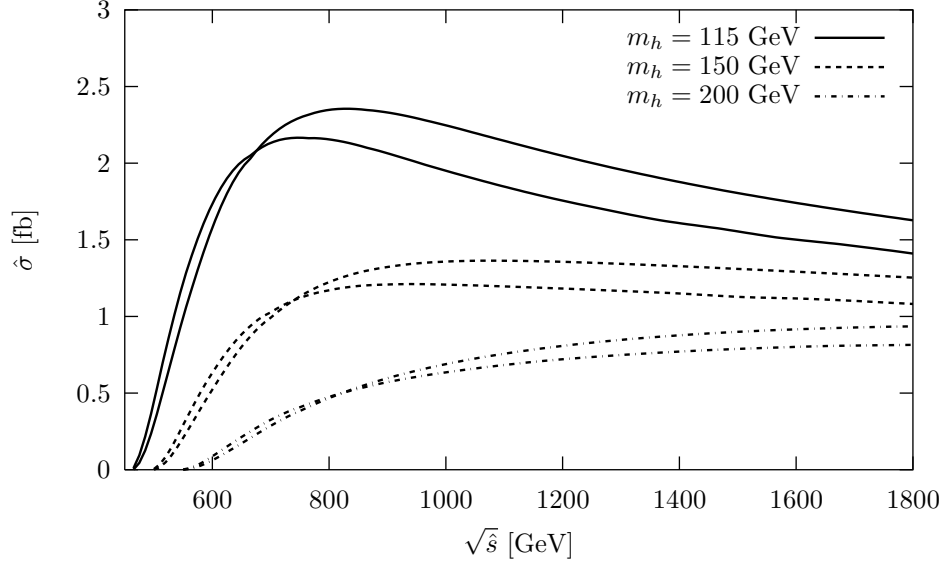


Figure 4: The Born and one-loop QCD corrected cross sections for the $\gamma\gamma \rightarrow t\bar{t}h^0$ subprocess as the functions of c.m.s. energy ($\sqrt{\hat{s}}$) with $m_h = 115, 150, 200$ GeV, respectively. For each line type, the upper curve(in the energy region $\sqrt{\hat{s}} > 1$ TeV) is for the Born cross section and the lower one for the one-loop QCD corrected cross section.

m_h (GeV)	$\sqrt{\hat{s}}$ (GeV)	$ \hat{\delta} _{max}(\%)$
115	1000	7.98
130	950	9.15
150	890	11.5
170	820	14.0
200	710	16.5

Table 1: The maximum electroweak absolute relative corrections and the corresponding colliding energy $\sqrt{\hat{s}}$ positions for the $\gamma\gamma \rightarrow t\bar{t}h^0$ subprocess with $m_h = 115, 130, 150, 170, 200$ GeV, respectively.

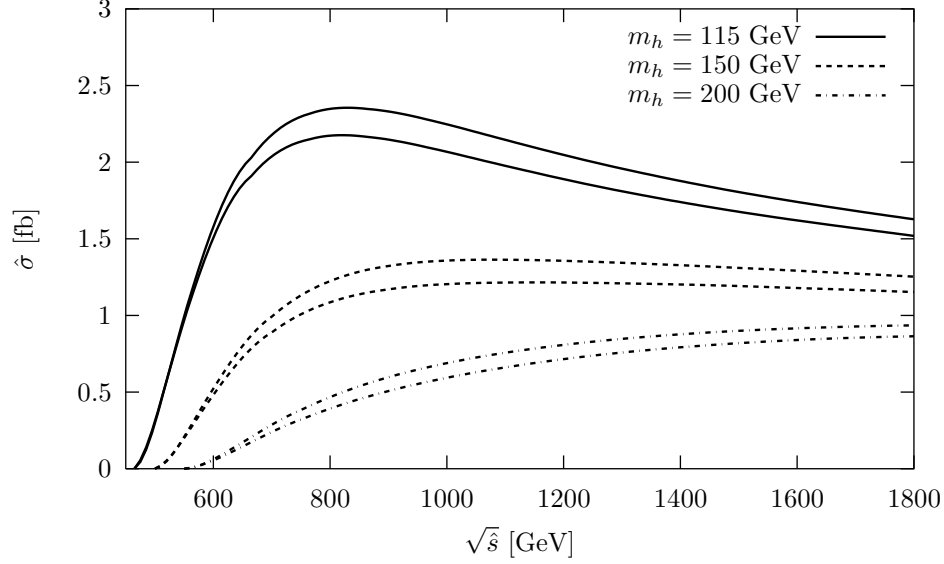


Figure 5: The Born and one-loop electroweak corrected cross sections for the $\gamma\gamma \rightarrow t\bar{t}h^0$ subprocess as the functions of c.m.s. energy ($\sqrt{\hat{s}}$) with $m_h = 115, 150, 200$ GeV. For each line type, the upper curve is for the Born cross section and the lower one for the one-loop electroweak corrected cross section.

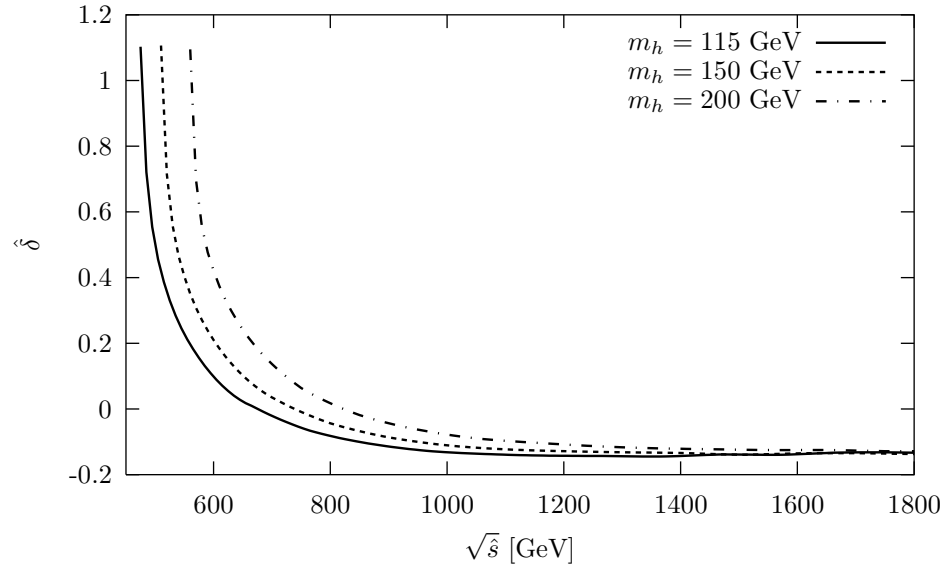


Figure 6: The QCD one-loop relative corrections as the functions of c.m.s. energy ($\sqrt{\hat{s}}$) for the $\gamma\gamma \rightarrow t\bar{t}h^0$ subprocess with $m_h = 115, 150, 200$ GeV, respectively.

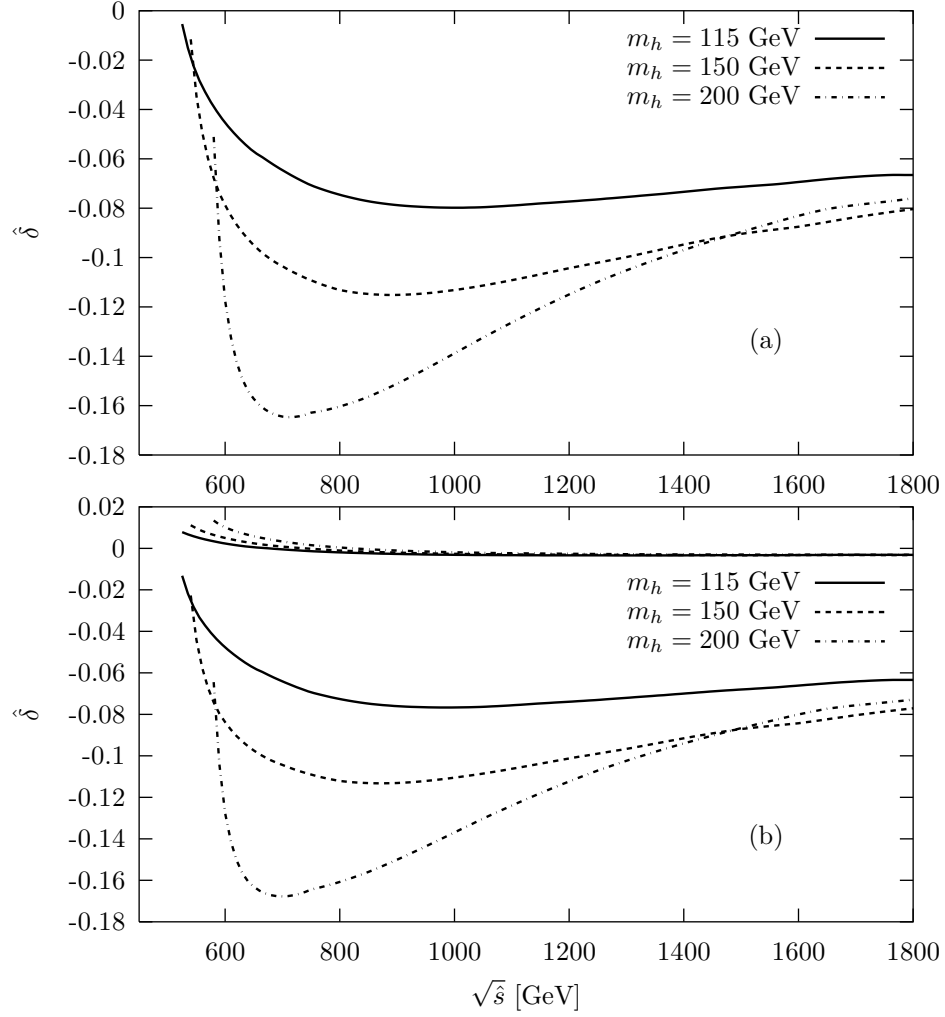


Figure 7: (a) The electroweak one-loop relative corrections as the functions of c.m.s. energy ($\sqrt{\hat{s}}$) with $m_h = 115, 150, 200$ GeV for the $\gamma\gamma \rightarrow t\bar{t}h^0$ subprocess. (b) The QED and weak one-loop relative corrections as the functions of c.m.s. energy ($\sqrt{\hat{s}}$) with $m_h = 115, 150, 200$ GeV for the $\gamma\gamma \rightarrow t\bar{t}h^0$ subprocess. For each line type, the upper curve is for the QED corrected cross section and the lower one for the weak corrected cross section.

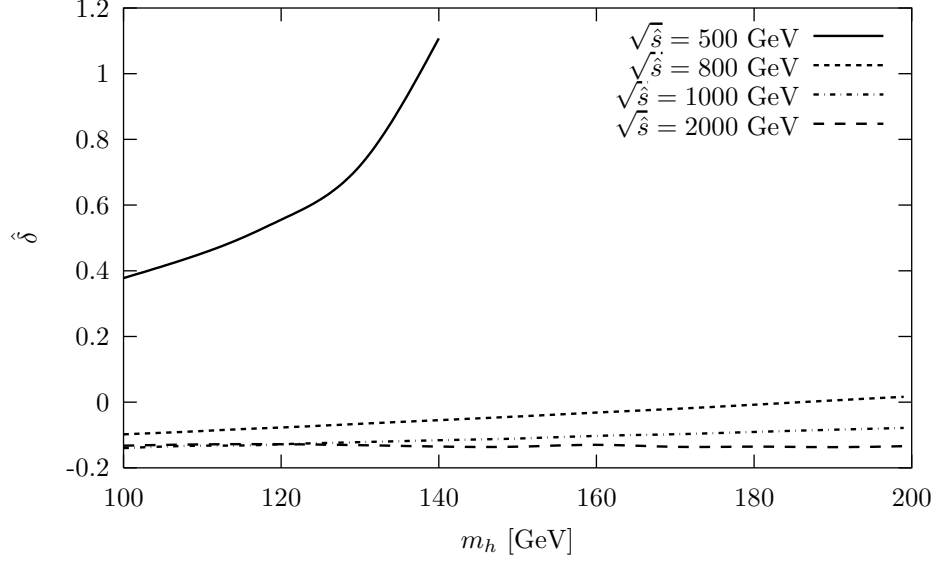


Figure 8: The QCD relative corrections to the cross sections of $\gamma\gamma \rightarrow t\bar{t}h^0$ subprocess as the functions of the mass of Higgs boson (m_h) with $\sqrt{\hat{s}} = 500, 800, 1000, 2000$ GeV, respectively.

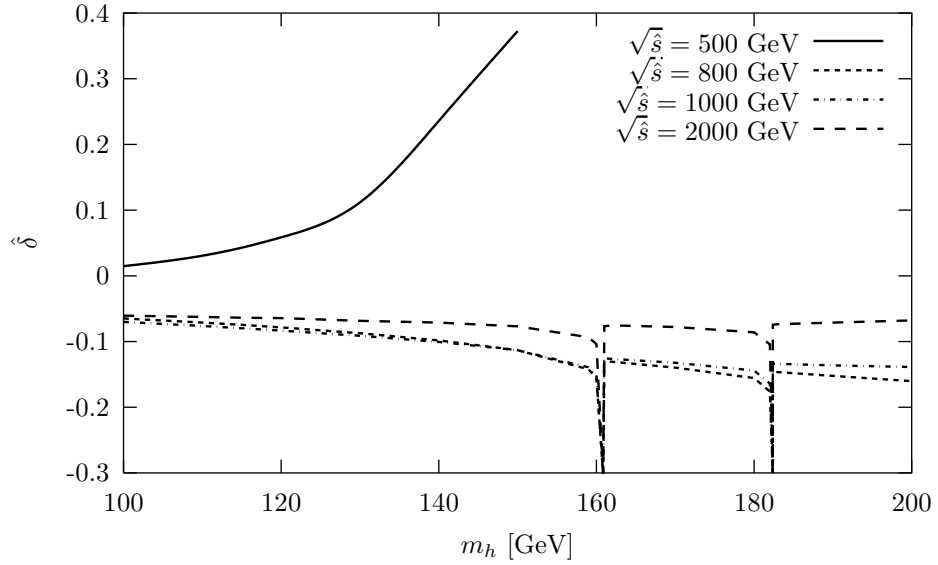


Figure 9: The electroweak relative corrections to the cross sections of $\gamma\gamma \rightarrow t\bar{t}h^0$ subprocess as the functions of the mass of Higgs boson (m_h) with $\sqrt{\hat{s}} = 500, 800, 1000, 2000$ GeV, respectively.

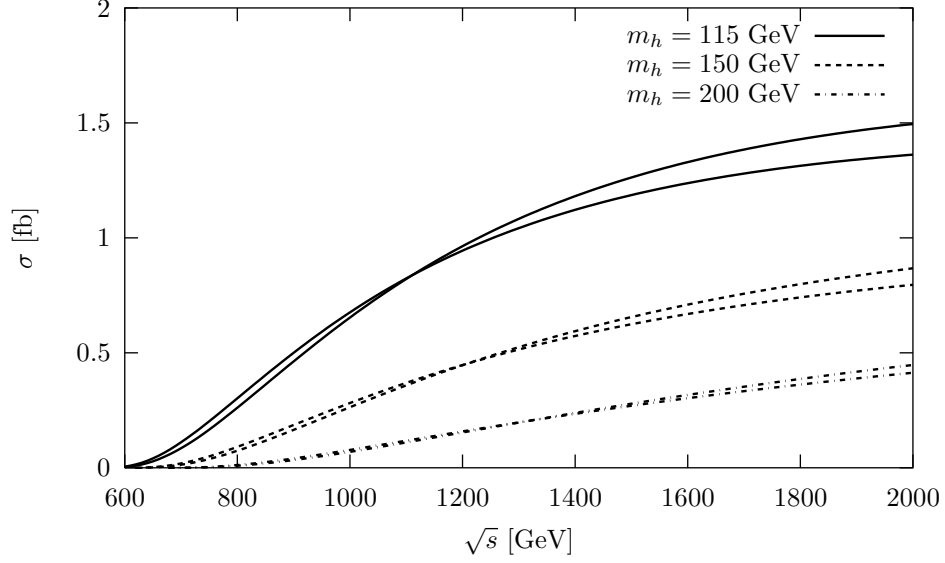


Figure 10: The Born and one-loop QCD corrected cross sections for the $e^+e^- \rightarrow \gamma\gamma \rightarrow t\bar{t}h^0$ process as the functions of c.m.s. energy (\sqrt{s}) with $m_h = 115, 150, 200$ GeV, respectively. For each line type, the upper curve (in the energy region $\sqrt{s} > 1.4$ TeV) is for the Born cross section and the lower one presents the one-loop corrected cross section.

m_h (GeV)	\sqrt{s} (GeV)	$ \delta _{max}(\%)$
115	2000	7.10
130	1700	8.28
150	1435	10.7
170	1220	13.4
200	1020	15.9

Table 2: The maximum absolute relative corrections and the corresponding colliding energy \sqrt{s} positions for the $e^+e^- \rightarrow \gamma\gamma \rightarrow t\bar{t}h^0$ process with $m_h = 115, 130, 150, 170, 200$ GeV, respectively.

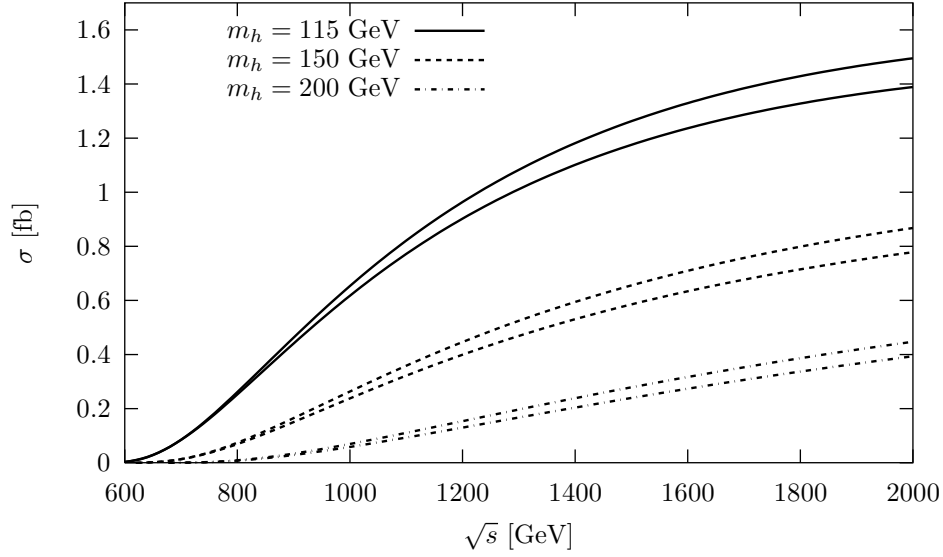


Figure 11: The Born and one-loop electroweak corrected cross sections for the $e^+e^- \rightarrow \gamma\gamma \rightarrow t\bar{t}h^0$ process as the functions of c.m.s. energy (\sqrt{s}) with $m_h = 115, 150, 200$ GeV, respectively. For each line type, the upper curve is for the Born cross section and the lower one presents the one-loop corrected cross section.

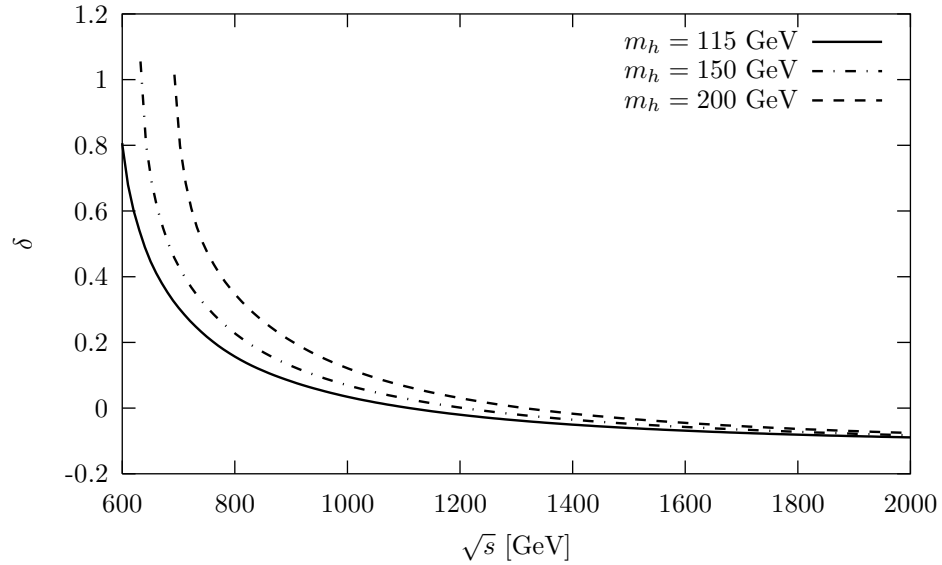


Figure 12: The QCD relative corrections to the $e^+e^- \rightarrow \gamma\gamma \rightarrow t\bar{t}h^0$ process as the functions of c.m.s. energy (\sqrt{s}) with $m_h = 115, 150, 200$ GeV, respectively.

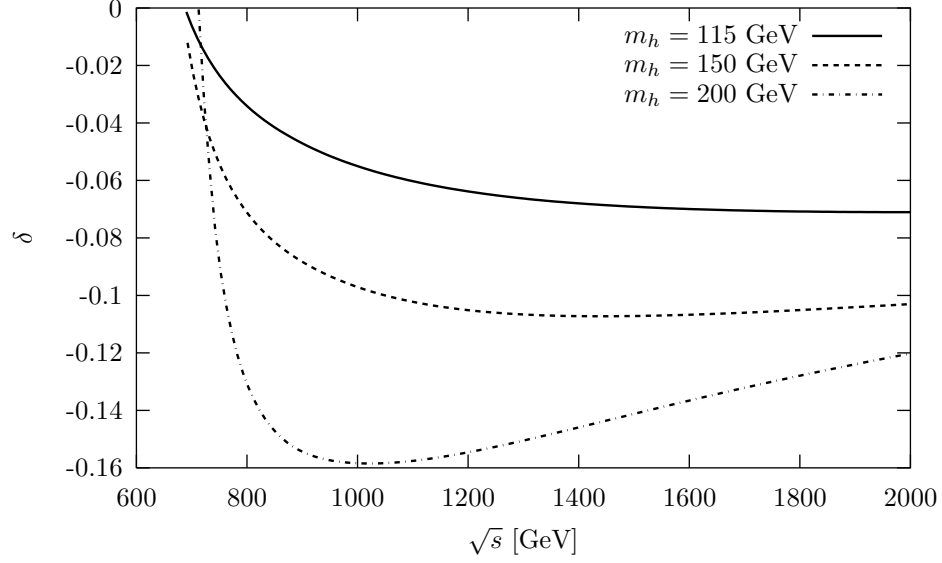


Figure 13: The electroweak relative corrections to the $e^+e^- \rightarrow \gamma\gamma \rightarrow t\bar{t}h^0$ process as the functions of c.m.s. energy (\sqrt{s}) with $m_h = 115, 150, 200$ GeV, respectively.

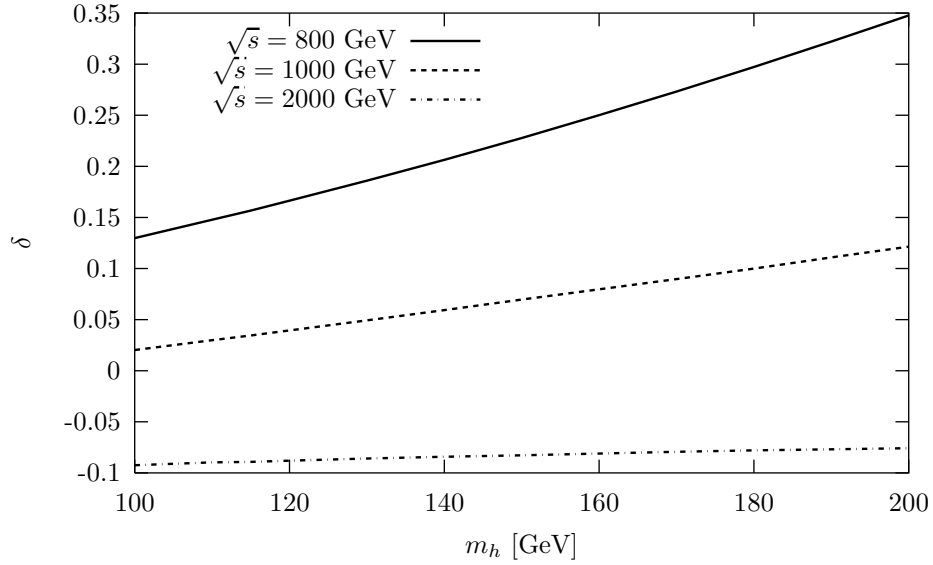


Figure 14: The QCD relative corrections to the $e^+e^- \rightarrow \gamma\gamma \rightarrow t\bar{t}h^0$ process as the functions of Higgs-boson mass (m_h) with $\sqrt{s} = 800, 1000, 2000$ GeV, respectively.

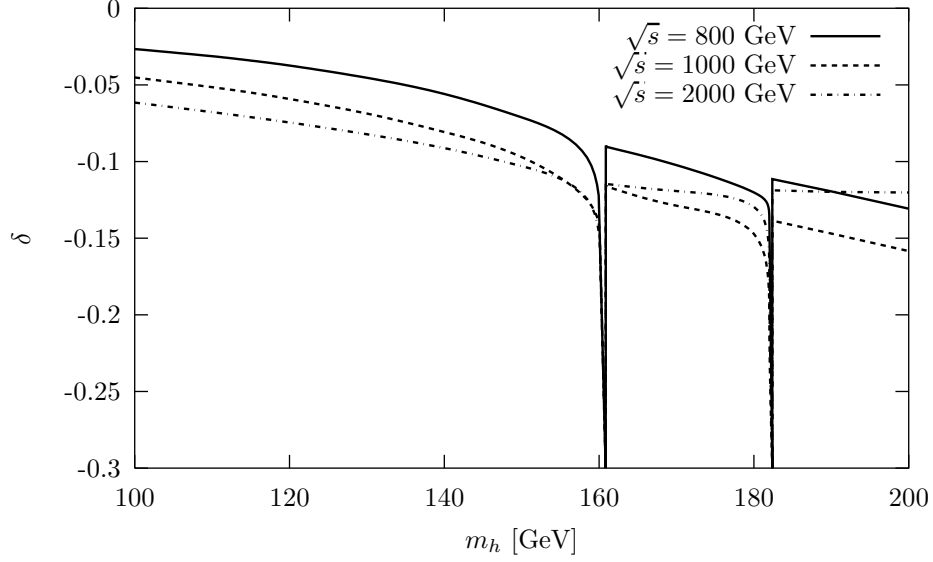


Figure 15: The electroweak relative corrections to the $e^+e^- \rightarrow \gamma\gamma \rightarrow t\bar{t}h^0$ process as the functions of Higgs-boson mass (m_h) with $\sqrt{s} = 800, 1000, 2000$ GeV, respectively.

m_t [GeV]	m_h [GeV]	\sqrt{s} [GeV]	σ [fb] (Ref.[18])	σ [fb] (FeynArts)	σ [fb] (CompHep)
120	60	500	0.45	0.3933	0.3918
		1000	2.6	2.188	2.191
		2000	2.8	2.391	2.391
150	60	1000	3.2	2.742	2.745
		2000	4.1	3.421	3.422
	140	1000	0.36	0.3118	0.3116
		2000	0.95	0.8067	0.8056
180	140	1000	0.40	0.3414	0.3415
		2000	1.2	1.0554	1.0552

Table 3: The numerical comparison of the cross sections of the process $e^+e^- \rightarrow \gamma\gamma \rightarrow t\bar{t}h^0$ at tree-level with the results in Ref.[18] by using FeynArts 3 and CompHep packages.